

Transcending the gain bandwidth limitation in semiconductors for full-colour-tunable lasers

Yi Jiang

Hong Kong Baptist University

Qi Wei

University of Macau <https://orcid.org/0000-0002-5322-3692>

King Fai Li

Hong Kong Baptist University

Mingke Jin

Southern University of Science and Technology

Hoi Lam Tam

Hong Kong Baptist University

Guixin Li

Southern University of Science and Technology <https://orcid.org/0000-0001-9689-8705>

Guichuan Xing

University of Macau

Kok Wai Cheah (✉ kwcheah@hkbu.edu.hk)

Hong Kong Baptist University <https://orcid.org/0000-0002-5226-2040>

Article

Keywords: Feedback Resonators, Discrete Lasing Wavelengths, Förster Resonance Energy Transfer, Guest-host Blends, Optoelectronic Devices

Posted Date: June 14th, 2021

DOI: <https://doi.org/10.21203/rs.3.rs-445403/v1>

License:  This work is licensed under a Creative Commons Attribution 4.0 International License.
[Read Full License](#)

Transcending the gain bandwidth limitation in semiconductors for full-colour-tunable lasers

Yi Jiang,^{1,4} Qi Wei,^{2,4} King Fai Li,^{1,3,4} Mingke Jin,³ Hoi Lam Tam,¹ Guixin Li,³ Gui-Chuan Xing,^{2*}

and Kok Wai Cheah^{1*}

¹Department of Physics and Institute of Advanced Materials, Hong Kong Baptist University, Kowloon Tong, Hong Kong SAR, China

²Institute of Applied Physics and Materials Engineering, University of Macau, Macao SAR 999078, China

³Department of Materials Science and Engineering, Southern University of Science and Technology, 518055, Shenzhen, China

⁴These authors contributed equally: Yi Jiang, Qi Wei, King Fai Li.

*e-mail: gcxing@um.edu.cn; kwcheah@hkbu.edu.hk.

ABSTRACT

Developing semiconductors with wide tunable gain bandwidth have always been at the forefront of laser technologies. The variation in feedback resonators can provide a useful tool for producing a relatively wide range of discrete lasing wavelengths. However, the lasing wavelength range is limited by the fundamental gain bandwidth of the single semiconductor itself. Full-colour range lasing through gain bandwidth tuning remains a daunting challenge. Here we demonstrate the feasibility of dynamically tuning amplification/lasing wavelengths in the entire emission spectrum by leveraging on Förster resonance energy transfer (FRET)-assisted guest-host blends. The unprecedented tunability in amplification and lasing is governed by energy transfer process, which enables us to achieve wavelength-tunable semiconductor lasers spanning the full visible region of the electromagnetic spectrum. Our distributed feedback lasers cover almost all CIE colour gamut (94%), which is 170% more perceptible colours than standard Red Green Blue colour space. These insights can guide the versatile and convenient design of semiconductor materials transcending current gain bandwidth limitation, paving the way for next generation of optoelectronic devices.

Introduction

Semiconductor laser opens the gate to laser miniaturization, and yields more compact and higher integrated optoelectronic devices. It enables the maturation of a wide range of new technologies, such as, optical fiber communications, image scanning, compact disc players, barcode scanners, laser printers, and compact LIDAR systems, with the development of gain materials, optics, and electronics¹⁻⁴. Tunable lasing wavelength region, arising from specific application requirements, is a key parameter of semiconductor laser. However, the fundamental gain bandwidth of a single semiconductor itself limits the range of discrete lasing wavelengths that a semiconductor can produce. Although engineered bandgaps have been demonstrated in traditional II-IV and III-V inorganic semiconductor alloys⁵⁻⁷, and inorganic and hybrid perovskite alloys⁸⁻¹⁰, the inevitable lattice mismatch issue, sophisticated fabrication technology, and imprecise composition control severely restrict the range of achievable bandgaps from the semiconductor alloys¹¹. In fact, semiconductors with wide tunable gain bandwidth would make revolutionary advances in optoelectronics.

Unlike inorganic semiconductors and perovskites, organic semiconductors have the abundant energy levels and thus can form multiple radiative channels arising from electronic-vibrational coupling¹²⁻¹⁵. This enables them theoretically ideal materials with wide gain bandwidth for continuously tunable laser application. With quasi-four level laser system for population inversion, the amplification generally occurs in the emission region with high Franck-Condon activity. In most cases, the gain bandwidth of organic gain medium is from 0-1 vibronic transition¹⁶⁻¹⁹, corresponding to an optimum and stable quasi-four level laser system. The distinct gain bandwidth has enabled lasing in a relatively wide range of discrete wavelengths but has not led to continuous tuning in the entire emission spectrum²⁰⁻²². A novel approach that utilize the abundant energy levels of organic semiconductors to overcome the gain bandwidth limitation is an attractive alternative, especially

considering its enormous potential in integrating into optoelectronic circuits^{23, 24}.

Here, we present a new strategy to tune the effective gain region across the emission spectrum by constructing Förster resonance energy transfer (FRET)-assisted guest-host gain system. FRET mechanism describes the energy from the host compound by light absorption, initially in its electronic excited state, could be resonantly and non-radiatively transferred to the guest compound. Taking the advantages of efficient excitation, suppressed concentration quenching, and reduced self-absorption, ultralow amplified spontaneous emission (ASE)/lasing thresholds have been demonstrated in guest-host gain systems with efficient and completed energy transfer²⁵⁻²⁹. Here we show the feasibility of continuously tunable light amplification across the optical range from polymeric guest-host gain systems. The key to successfully tune the gain bandwidth across the optical range is manipulating the energy transfer efficiency. Different host/guest ratio produces a shift in the energy transfer preference of the blended compound, and therefore the energy transfer efficiency would change with respect to the blending ratio. These changes create different meta-stable energy environments for light amplification and thus novel effective gain regions, leading to the wavelength tunability in light amplification. We assume that the individual host or guest compound holds a typical quasi-four level laser system with optical gain region at its 0-1 vibronic transition. With FRET taking place in the process, at least five different energy environments for light amplification can be created with possible stimulated emission channels in both guest and host (Fig. 1a). Combining with distributed feedback (DFB) resonating modulation, the full-colour range of continuously tunable lasing is achievable in these guest-host blends.

Tunable ASE in guest-host gain systems

The guest-host gain systems we studied consist commercial polymers, poly(9,9-dioctylfluorene) (PFO), poly(2-(2'-5'-bis(2''-ethylhexyloxy)phenyl)-1,4-phenylene-vinylene) (BEHP-PPV), and

poly(2-methoxy-5-(2-ethylhexyloxy)-1,4-phenylene-vinylene) (MEH-PPV) (Fig. 1b). These polymers, as amorphous morphology film, exhibit some typical characteristics of organic gain media¹⁹, such as, optical absorption coefficient (α) of $\sim 10^5 \text{ cm}^{-1}$ at the maximum absorbance, well-resolved emission bands from 0-0 to 0-2 (or 0-3) vibronic transitions, moderate photoluminescence (PL) quantum yield (PLQY), amplification at its 0-1 vibronic transition channel, and acceptable ASE threshold (Fig. 1c, Supplementary Figs. 1-3 and Table 1). The PLQY values of 50%, 20%, and 9% are obtained for PFO, BEHP-PPV, and MEH-PPV, respectively, with excitation at 390 nm. MEH-PPV, BEHP-PPV, and PFO waveguide structures demonstrate the independent red, green, and blue (RGB) ASE. The ASE thresholds of individual PFO, BEHP-PPV and MEH-PPV films are $11.4 \mu\text{J}/\text{cm}^2$, $7.7 \mu\text{J}/\text{cm}^2$, $77.1 \mu\text{J}/\text{cm}^2$, respectively, under 355 nm, 10 Hz, 5 ns pulsed laser excitation. There is a good overlap between PFO (or BEHP-PPV) emission spectrum and BEHP-PPV (or MEH-PPV) absorption spectrum, indicating efficient energy transfer between PFO and BEHP-PPV, and between BEHP-PPV and MEH-PPV. Two blend systems, PFO:BEHP-PPV and BEHP-PPV:MEH-PPV, were investigated as guest-host gain systems.

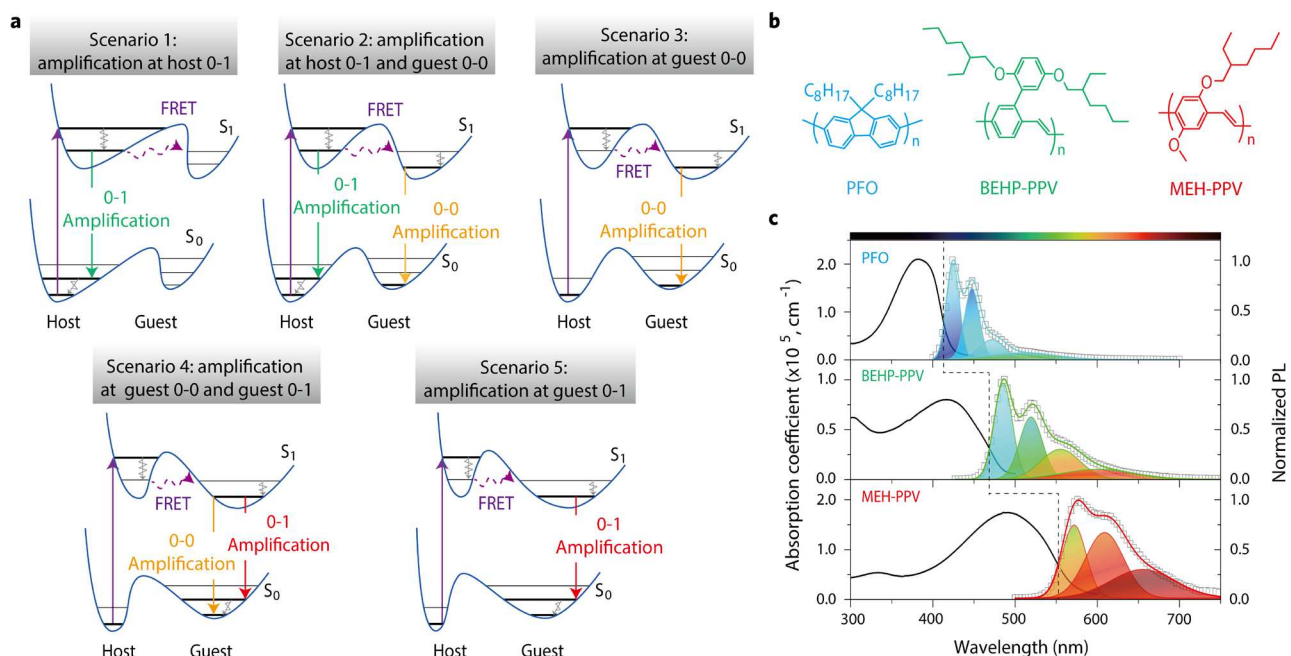


Figure 1 | Energy diagram, polymer chemical structures and glass film optical properties. a,

Guest-host gain system with possible stimulated emission energy levels in both guest and host, with FRET taking place in the process. **b**, Polymer chemical structures of PFO, BEHP-PPV, and MEH-PPV. **c**, Absorbance (black solid line, left) and PL (grey open squares, right) spectra of PFO, BEHP-PPV, and MEH-PPV films. The PL spectra are fitted by multi-Lorentzian-function to determine different emission bands (filled area). The cumulative fits for PFO, BEHP-PPV, and MEH-PPV are blue, green, and red lines, respectively.

A systematic study was carried out on the light amplification characteristics of BEHP-PPV:MEH-PPV blended samples with different host/guest ratios. The guest (MEH-PPV) weight concentrations are varied from 0% to 40%. The blended polymers were deposited by spin-coating the mixed solutions on quartz substrates to form \sim 150 (\pm 30) nm-thick smooth films. Clear signatures of tunable light amplification, that is, green, green and yellow (dual-wavelengths), yellow, yellow and red (dual-wavelengths), and red ASE phenomena, are observed in BEHP-PPV:MEH-PPV blend system (Fig. 2a). With increasing MEH-PPV concentration, the absorption band at \sim 500-560 nm from MEH-PPV increases progressively (Supplementary Fig. 4). At low MEH-PPV concentrations (less than 4%), the PL spectra of the blended polymers clearly include the characteristic green emission from BEHP-PPV and the distinct emission bands from MEH-PPV (Supplementary Fig. 5). The green PL emission vanishes gradually when MEH-PPV concentration is over 4%, implying the near completed energy transfer processes in these blending ratios. The chromaticity of the blended polymers on the CIE 1931 coordinate diagram shows that the colour moves from green, across the yellow region, to red with increasing MEH-PPV concentration (Fig. 2b). The wide chromaticity variation in PL, accompany with the change of energy environments for light amplification, leads to the entirely different ASE behaviours.

The onset of ASE is manifested as the emergence of narrow features; first emerged in the yellow

region (\sim 562 nm), and then appeared at the 0-1 vibronic transition channel of host with emission peak at 523 nm with increasing pump fluence in BEHP-PPV:MEH-PPV 99.8:0.2 (Supplementary Fig. 6). This is accompanied by nonlinear increase in emission intensity with well-defined thresholds of 48.4 and 40.1 $\mu\text{J}/\text{cm}^2$ for the green and yellow ASE features, respectively (Fig. 2c). Similar dual-wavelengths ASE phenomenon with gain bandwidths in both yellow and red is observed by adjusting the host/guest ratio to 98:2 (Fig. 2c and Supplementary Fig. 7). These tunable gain bandwidths originate from the competing stimulated emission at several vibronic transition channels in both guest and host, which is created from the variation of energy environments for light amplification. By tuning the blending ratio, the single-wavelength amplification in yellow or red region is also observed in the blended polymers (Supplementary Figs. 8 and 9).

Figs. 2d and 2e depict the dependence of ASE threshold(s) and peak(s) in each MEH-PPV concentration in BEHP-PPV:MEH-PPV blended samples with ASE in green, yellow, and red regions, respectively. Green ASE thresholds raise sharply from 7.7 $\mu\text{J}/\text{cm}^2$ to \sim 200 $\mu\text{J}/\text{cm}^2$, contrary to the increase in PLQY values (Supplementary Fig. 10), by slightly increasing dopant concentration even with low concentration level \leq 0.4% in the blended polymers. FRET process provides radiative transition channels in guest; this reduces the exciton density in the host gain region, therefore it is unfavourable for population inversion in host gain region. Spectral narrowing in yellow region are observed in the blended samples with MEH-PPV concentrations larger than 0.2%. The lowest yellow ASE threshold of 15 $\mu\text{J}/\text{cm}^2$ is obtained in BEHP-PPV:MEH-PPV 98:2. Similarly to yellow amplification phenomena that we have observed, very low red ASE thresholds (\sim 4 $\mu\text{J}/\text{cm}^2$) are obtained in the blended samples with MEH-PPV concentrations between 6% and 10%. The amplification characteristics of all BEHP-PPV:MEH-PPV blended samples are summarized in Supplementary Table 2. As a point of comparison, the measured ASE thresholds obtained here are

among the lowest values reported in dendritic starbursts³⁰, polymers^{31, 32}, and guest-host gain systems^{28, 29, 33, 34} with yellow or red amplification under nanosecond pulse excitation. Intriguingly, the peaks of green amplification in the blended polymers do not show any shift with respect to the blending ratio (Fig. 2e). However, the peaks of yellow and red amplification undergo bathochromic shifts (varying from 562 nm to 577 nm and from 600 nm to 618 nm, respectively) with increasing dopant concentration in BEHP-PPV:MEH-PPV blend system. The overlap between 0-2 vibronic band of host and 0-0 vibronic band of guest renders the designation of yellow gain region indistinguishable (Fig. 1c). With the gradual bathochromic shifts of yellow and red amplification synchronizing with the occurrence of enhanced guest molecule aggregation, we propose that the yellow and red amplification are associated to the 0-0 and 0-1 radiative channels of guest.

Tunable amplification, covering blue, blue and sky-blue (dual-wavelengths), sky-blue, sky-blue and green (dual-wavelengths), and green ASE, is demonstrated in PFO:BEHP-PPV blend system, which also shows the generality of tunable gain bandwidth in FRET-assisted guest-host gain systems (Supplementary Figs. 11-18 and Table 3). BEHP-PPV:MEH-PPV blend system is used as the main example for further discussion on energy transfer process and stimulated emission cross-section simulations.

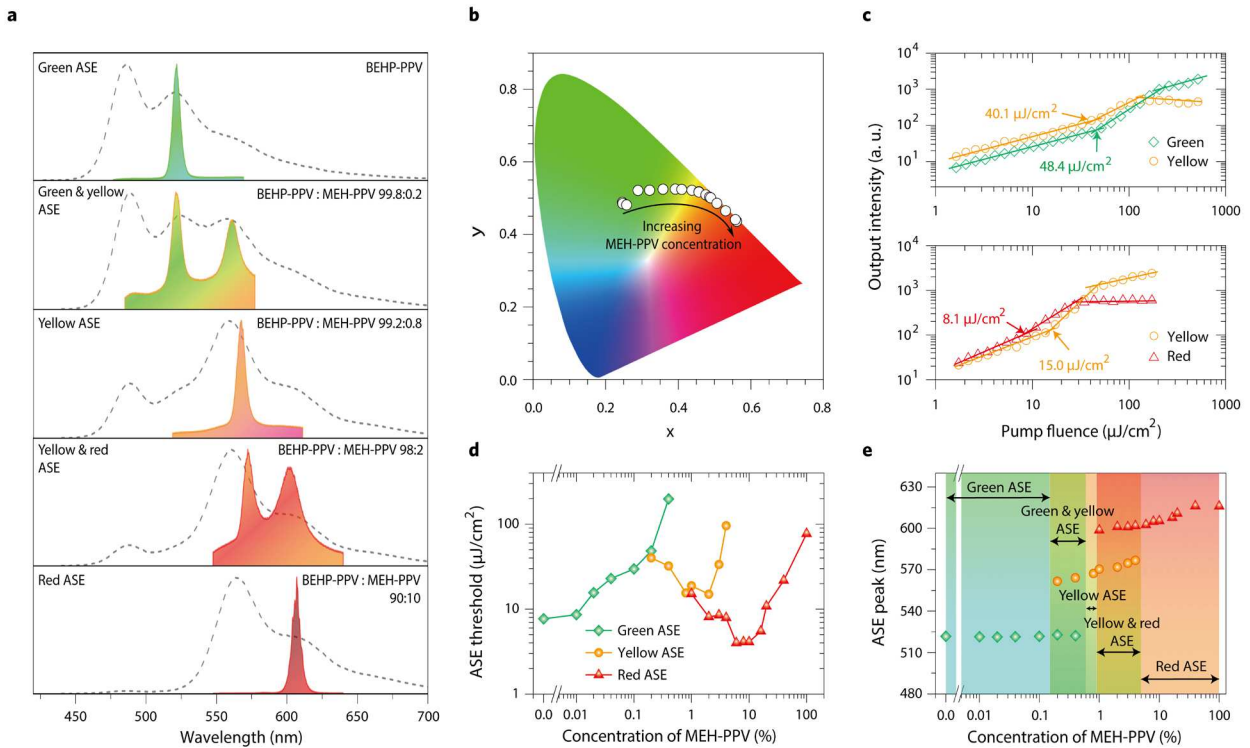


Figure 2 | ASE characteristics of BEHP-PPV:MEH-PPV blend system. **a**, Wavelength tunability in amplification in BEHP-PPV:MEH-PPV blended samples with different MEH-PPV concentrations. The corresponding PL spectra of the samples are also shown with gray dash line. **b**, Trajectory of colour modulation of fluorescence emission in the CIE coordinate diagram, as a function of MEH-PPV concentration in BEHP-PPV:MEH-PPV blended samples. **c**, Output intensity versus pump fluence for BEHP-PPV:MEH-PPV 99.8:0.2 (top panel) and BEHP-PPV:MEH-PPV 98:2 (bottom panel), representing the typical dual-wavelengths ASE, i.e., green and yellow ASE, and yellow and red ASE, respectively. **d**, Plots of ASE threshold(s) as a function of MEH-PPV concentration in the blend system with ASE in green, yellow, and red regions, respectively. **e**, Dependence of ASE central wavelength(s) on MEH-PPV concentration in the blend system. The amplification characteristics are divided into five zones with different effective gain regions.

Energy transfer process

To better understand the energy transfer process, time-resolved PL (TRPL) decay transients were recorded in BEHP-PPV:MEH-PPV blend system. In the absence of MEH-PPV, the TRPL decay

kinetics of BEHP-PPV manifest a bi-exponential decay profile with an average fluorescence lifetime of 141 ps (Figs. 3a and 3b). When MEH-PPV is blended with BEHP-PPV, a portion of MEH-PPV emission originates by transfer from BEHP-PPV, and the proposed energy transfer leads to the reduced BEHP-PPV emission and lifetime. The transient lifetime of BEHP-PPV in the blend system gradually decreases to only 11 ps, with progressively increasing MEH-PPV concentration to 10% (Fig. 3a). In fact transient lifetimes are inversely proportional to the rates of exciton transfer and relaxation. Energy transfer efficiency >90% is obtained with MEH-PPV concentration higher than 10%. The tuning of energy transfer rates in a broad range ($2.0 \times 10^8 \text{ s}^{-1}$ - $1.6 \times 10^{11} \text{ s}^{-1}$) is achieved through varying the blending ratios (Fig. 3c and Supplementary Table 4). Not only does it provide the route to change the energy environments for emission and amplification, but it also makes it possible to overcome the limitation of the fundamental gain bandwidths of guest and host themselves.

To gain further insight into FRET dynamics between guest and host excited states, we performed pump-probe transient absorption (TA) spectroscopy experiments on BEHP-PPV:MEH-PPV blended samples as a function of excitation density. The blended samples with MEH-PPV concentrations of 0%, 0.1%, 1%, 2%, 4%, and 10% are subjected to TA measurements with an excitation density of 9.5 $\mu\text{J}/\text{cm}^2$, which is below the gain thresholds of all samples under femtosecond pulse excitation. The representative TA spectra of these samples over the same spectral region show the pronounced photobleaching (PB) bands and a photoinduced absorption (PIA) band (Fig. 3d and Supplementary Fig. 19). For BEHP-PPV, the PB bands are attributed to the ground state absorption and stimulated emission from its first excited singlet state³⁵. The contributions to the PB bands of the blended samples are comprised of ground state absorption and stimulated emission of both guest and host, and the results at each time delay are shown as a simple combination thereof (Supplementary Fig. 19). The corresponding PIA bands are assigned to weakly coupled polaron-pair charge states of host,

similar to other polymers³⁶⁻³⁸, with the dominated wavelength region in 650-750 nm. The PIA signals in these blended samples are formed rapidly (<200 fs) before decaying with average time constants of ~1 ns (Fig. 3e, Supplementary Fig. 20 and Table 5). As a result of the increased MEH-PPV stimulated emission from FRET competing with host PIA, the isosbestic points at 1 ps delay are red-shifted from 615 nm to 670 nm with increasing dopant concentrations to 10% in BEHP-PPV:MEH-PPV blend system (Fig. 3d). The negligible overlap between host PIA and effective gain regions indicates the insignificant influence of BEHP-PPV polaron-pair formation on stimulated emission in BEHP-PPV:MEH-PPV blend system³⁸. Thus it is possible to observe the energy migration between guest and host from the TA spectra of these blended samples without considering the host PIA.

TA kinetics of BEHP-PPV at sky-blue, green, and yellow PB regions reveal the similar rise time, which is consistent with the same excitation pathway for different vibronic transition channels (0-0 to 0-2) in an individual polymer. After FRET taking place in the process, the transient kinetics of these blended samples at different regions are much different (Fig. 3e and Supplementary Fig. 20). As an example, fast PB buildup for sky-blue and green regions with rise time of 1.5 ps and 2.3 ps are manifested in BEHP-PPV:MEH-PPV 98:2 (Fig. 3e). Subsequently, the sky-blue and green transients begin to decay, which match well with concomitant rises of the PB signals at yellow and red regions, both at 5-10 ps. The stimulated emission at red region, which is assigned to guest 0-1 radiative channel, is formed slowest, in good agreement with the occurrence of FRET. The moderate kinetics at yellow region are anticipated, depending on its vibronic transition channels in both guest and host. The properties of TA kinetics of these blended samples under this excitation density condition are summarized in Supplementary Table 5.

The dynamics of energy migration under amplification condition were captured in TA kinetics at different PB regions by enhancing the excitation densities. When BEHP-PPV:MEH-PPV 98:2 is

pumped under an excitation density of $38.2 \mu\text{J}/\text{cm}^2$ (with yellow ASE output; Supplementary Fig. 21), the promptly formed PB signals at sky-blue and green regions with rise time of 0.70 ps and 0.85 ps exhibit excited-state decay that is kinetically correlated with the formation of PB signal at yellow region (Fig. 3f). Complementary kinetics under a higher excitation density ($56.0 \mu\text{J}/\text{cm}^2$) with dual-wavelengths ASE in green and yellow regions present shorter rise time and similar lag in the formation of PB signals between host regions (sky-blue and green) and yellow region (Fig. 3g). The distinct lag of rise time in host regions and yellow region are also observed in other blended samples with yellow, yellow and red (dual-wavelengths), and red ASE under femtosecond pulse excitation (Supplementary Figs. 21-24, and Table 6). These experiments illustrate that yellow ASE readily proceeds from guest 0-0 radiative channel, exhibiting behavior characteristics of guest in guest-host gain system. Note that the short laser pulse width (100 fs), which is even shorter than FRET time, is adverse to the exciton accumulation in guest gain regions for population inversion. The ASE characteristics of BEHP-PPV:MEH-PPV blended samples under femtosecond pulse excitation are distinctive in comparison with that under nanosecond pulse excitation. The relatively higher MEH-PPV concentrations are demanded to achieve the gain bandwidths in yellow and red regions under femtosecond pulse excitation in comparison with the results under nanosecond pulse excitation (Supplementary Fig. 21).

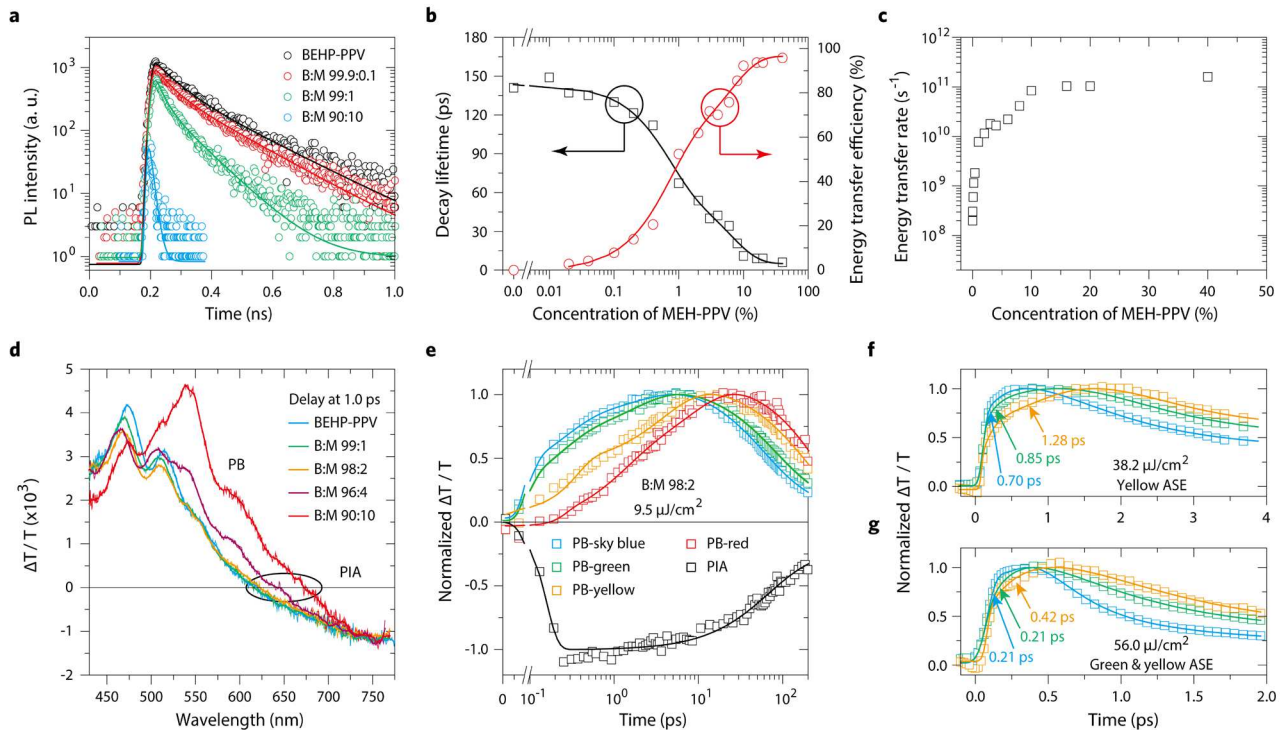


Figure 3 | Photophysical characterization of BEHP-PPV:MEH-PPV (B:M) blended samples. **a**, TRPL decay characteristics of B:M blended samples at host emission region (~ 487 nm). **b**, Host decay lifetime and energy transfer efficiency plotted versus MEH-PPV concentration for B:M blend system. **c**, The rates of energy transfer deduced from TRPL decay kinetics for B:M blends. **d**, TA spectra of B:M blended samples after excitation at 400 nm (1 kHz, 100 fs, $9.5 \mu\text{J}/\text{cm}^2$) at 1 ps. The ellipse highlights the isosbestic points in the TA spectra. **e-g**, Normalized kinetics of B:M 98:2 at different PB (and PIA) regions under different excitation densities ($9.5 \mu\text{J}/\text{cm}^2$, **e**; $38.2 \mu\text{J}/\text{cm}^2$, **f**; $56.0 \mu\text{J}/\text{cm}^2$, **g**). The PB region is 482-492 nm for sky-blue, 517-527 nm for green, 566-576 nm for yellow, and 598-608 nm for red. The PIA region is 710-730 nm.

The effective stimulated emission cross-section simulations

The simulations of effective stimulated emission cross-sections at different colour regions provide an insight to observe the influence of energy environment changes on light amplification in BEHP-PPV:MEH-PPV blend system that cannot be obtained from experimental measurement. An analysis of the contribution ratios of effective stimulated emission cross-sections from possible radiative

channels in both guest and host of the blended samples can provide further evidence for their designation to respective gain regions. In addition, it can assist the blending ratio selection for amplification in specific colour(s). Here, we performed the simulations by considering stimulated emission cross-sections and possible absorption cross-sections (see Methods, Supplementary Figs. 25 and 26). The effective stimulated emission cross-section of BEHP-PPV is $3.31 \times 10^{-16} \text{ cm}^2$ at 0-0 vibronic band, $3.64 \times 10^{-16} \text{ cm}^2$ at 0-1 vibronic band, $1.80 \times 10^{-16} \text{ cm}^2$ at 0-2 vibronic band, and $9.57 \times 10^{-17} \text{ cm}^2$ at 0-3 vibronic band (Supplementary Fig. 26). The corresponding contribution ratios of effective stimulated emission cross-sections at sky-blue, green, yellow, and red regions are 0.341, 0.375, 0.186, and 0.098, in agreement with its green ASE (Fig.4 and Supplementary Fig. 27). With the slight increase in blending ratio (the range of MEH-PPV concentration: 0-2%), the effective stimulated emission cross-sections at host radiative channels decrease gradually. On the contrary, the concomitant effective stimulated emission cross-sections at guest 0-0 and 0-1 vibronic bands are significantly enhanced in this process. When MEH-PPV concentration is higher than 6%, there is no contribution from host radiative channels anymore, corresponding to the near vanished emission from host and energy transfer efficiencies >80%. The highest effective stimulated emission cross-sections at guest 0-0 and 0-1 vibronic bands in the blend system are demonstrated as $5.72 \times 10^{-16} \text{ cm}^2$ and $5.00 \times 10^{-16} \text{ cm}^2$ with MEH-PPV concentrations at 3% and 8%, respectively (Supplementary Fig. 26). They match the lowest yellow and red ASE thresholds observed around these MEH-PPV concentrations³⁹.

Fig. 4 presents the contribution ratios of effective stimulated emission cross-sections of BEHP-PPV:MEH-PPV blended samples with MEH-PPV concentrations of 0%, 0.2%, 0.8%, 2%, and 10%, representing the typical green, green and yellow (dual-wavelengths), yellow, yellow and red (dual-wavelengths), and red ASE under nanosecond pulse excitation, respectively (Fig. 2a). The change of

energy environments for light amplification, i.e., the change of contribution ratios of effective stimulated emission cross-sections at different radiative channels, could be clearly observed in these blended samples. It is easy to decide that the contributions for effective stimulated emission cross-sections at yellow and red regions are dominated by guest 0-0 and 0-1 radiative channels. As an example, with MEH-PPV concentration at 0.8%, the contribution ratio from guest 0-0 vibronic band is 0.381, which is 6-fold higher than that from host 0-2 vibronic band. When MEH-PPV concentration is up to 2%, the contributions from host radiative channels at yellow and red regions are almost negligible. These results reveal that the construction of guest-host gain system is an effective strategy to achieve the tunable light amplification, beyond the limits of the fundamental gain bandwidths of guest and host themselves.

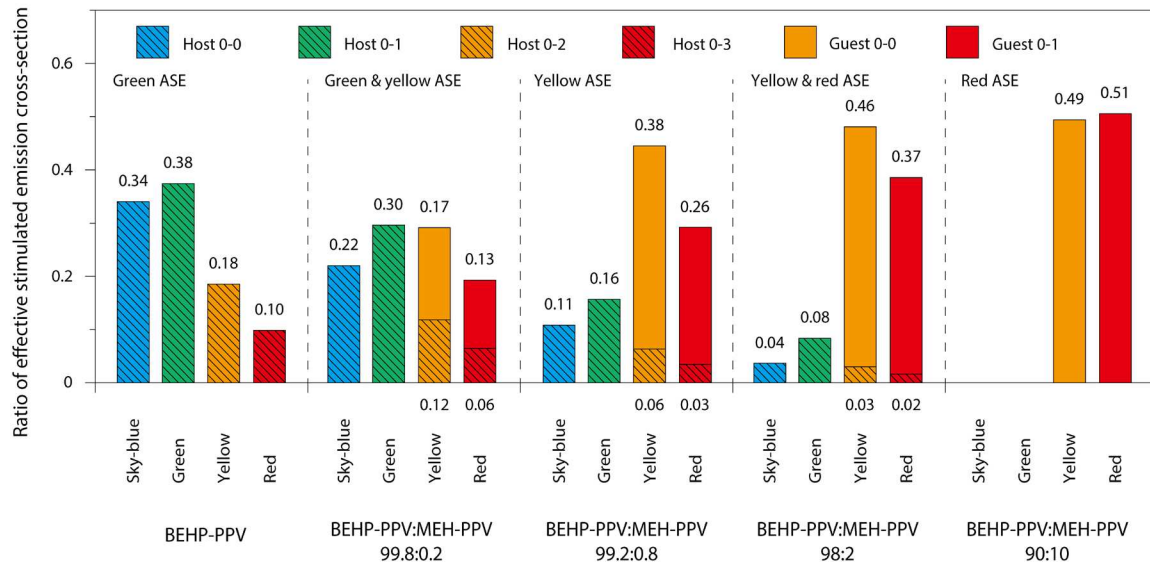


Figure 4 | The contribution ratio of effective stimulated emission cross-section for BEHP-PPV:MEH-PPV blended samples. The colour regions are sky-blue, green, yellow, and red. The corresponding contributions are from possible radiative channels in both guest and host.

Full-colour range tuning lasing

Distributed feedback (DFB) lasers were then conducted and fabricated by spin-coating PFO:BEHP-

PPV or BEHP-PPV:MEH-PPV blends on top of patterned silica gratings, to further demonstrate the wide range of continuously tunable lasing from our guest-host gain systems. The grating periods of 270 nm, 300 nm, 340 nm, 370 nm and 410 nm are selected for blue, sky-blue, green, yellow, and red DFB lasing outputs, respectively. Thus three second-order DFB gratings (Grating-1/2/3) and four mixed second-order DFB gratings (Grating-4/5/6/7) were prepared by electron beam lithography (Supplementary Section 6, Figs. 28-35). The latter are designed for one or more wavelength lasing. The details of DFB grating fabrication and the selection of gain media are presented in Supplementary Section 6. The summary of grating parameters and gain media are also listed in Table 1. Under optical excitation, continuously tunable lasing, that span the full visible region of the electromagnetic spectrum (from 450 nm to 619 nm), are achieved (Fig. 5a). Fig. 5b shows the derived chromaticity for these lasing spectra on a CIE colour diagram. The full-colour range tuning organic lasing cover 78% of CIE colour gamut, which is 120% more perceptible colours specified by CIE LAB colour space (standard Red Green Blue, sRGB)⁴⁰.

The lasing wavelength range could be further extended. For example, for RGB lasers, the lasing wavelengths are 450 nm, 523 nm, and 619 nm (Fig. 5a), with the corresponding lasing thresholds of 5.7 nJ/pulse, 5.1 nJ/pulse, 32.2 nJ/pulse (Fig. 5c). The results are attained with BEHP-PPV:MEH-PPV 90:10, PFO:BEHP-PPV 60:40, and PFO as gain media, respectively. Tuning the film thickness in the range 100-200 nm for PFO, 100-500 nm for PFO:BEHP-PPV 60:40, and 100-500 nm for BEHP-PPV:MEH-PPV 90:10 would produce lasing wavelengths across spectral windows of 439-457 nm, 500-541 nm, and 600-644 nm (Fig. 5d). The extended trajectory of tunable lasing colours in the CIE coordinate diagram through the variation of polymer film thicknesses shows that the colours cover approximately 170% more perceptible colours than sRGB (94% of CIE colour gamut; Supplementary Fig. 36). Although further studies will be needed to further fine characterize these

blend systems and optimize feedback resonators, this is to the best of our knowledge the widest tunable semiconductor laser system from three materials. Overall, these data demonstrate that our concept and realization of guest-host gain systems with wide tuning of gain bandwidth yield unprecedented wavelength tunability in semiconductor lasers.

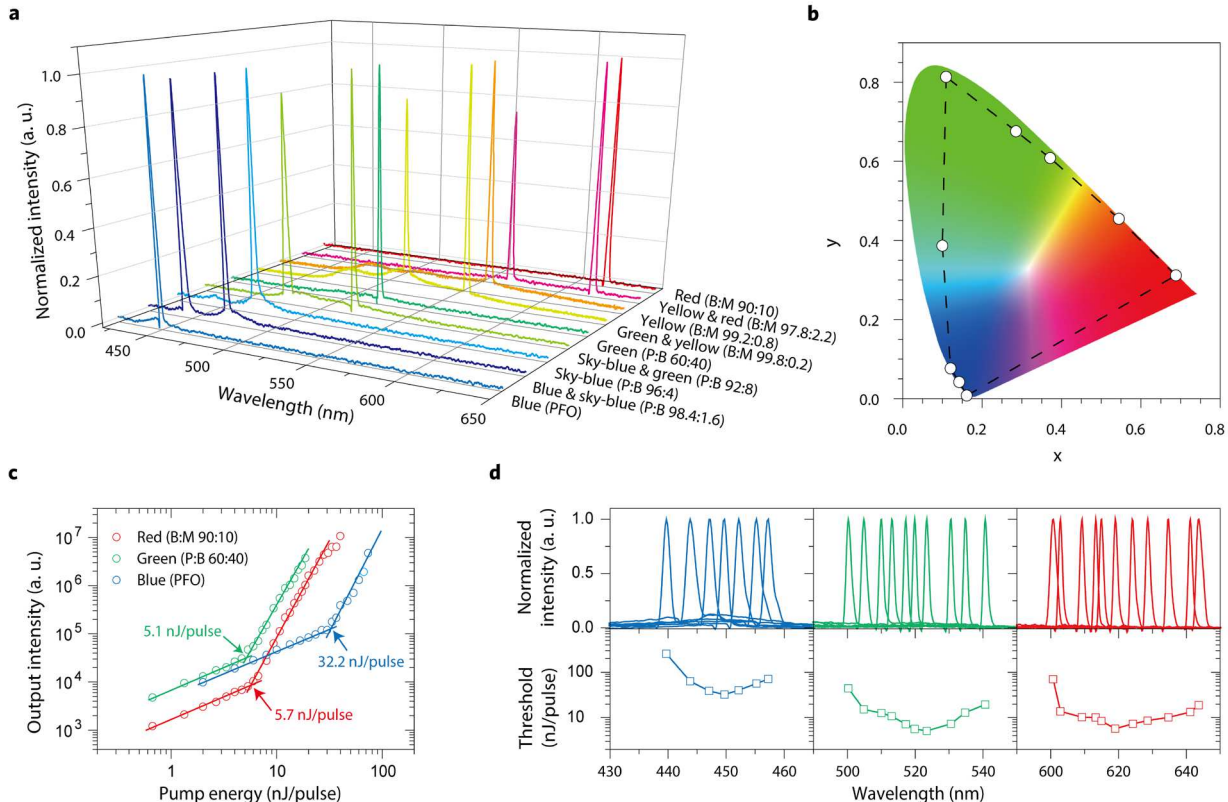


Figure 5 | Full-colour-tunable lasing. **a**, The tunable lasing spectra from PFO:BEHP-PPV (P:B) and BEHP-PPV:MEH-PPV (B:M) blends. **b**, Trajectory of tunable lasing colours extracted from figure **a** in the CIE coordinate diagram. Dash lines indicate the range of the achievable colour gamut for P:B and B:M blend systems. **c**, Log-log plot of output intensity versus pump energy in RGB DFB lasers (figure **a**) with lasing wavelengths at 450 nm, 523 nm, and 619 nm. The grating periods are 270 nm, 340 nm, and 410 nm, respectively. **d**, Top panels: Tuning the RGB lasing wavelength by varying the polymer film thickness (the same gain media and gratings in figure **c**). Film thicknesses in the range 100-200 nm for PFO, 100-500 nm for P:B 60:40, and 100-500 nm for B:M 90:10 give 439-457 nm, 500-541 nm, and 600-644 nm laser emission. Bottom panels: Dependence of lasing

threshold on wavelength.

Table 1. The information of DFB lasers.

Grating samples	Period (nm) ^[a]	Gain medium on the top ^[b]	Lasing colour(s)
Grating-1	270	PFO	Blue
Grating-2	340	P:B 60:40	Green
Grating-3	410	B:M 90:10	Red
Grating-4 ^[c]	270, 300	P:B 98.4:1.6	Blue and sky-blue
Grating-5 ^[c]	300, 340	P:B 96:4 P:B 92:8	Sky-blue Sky-blue and green
Grating-6 ^[c]	340, 370	B:M 99.8:0.2	Green and yellow
Grating-7 ^[c]	370, 410	B:M 99.2:0.8 B:M 98:2	Yellow yellow and red

^[a] The etched depth is 80 nm for all grating samples. ^[b]The gain media are spin-coated on top of patterned silica gratings. P:B or B:M represents the blended sample with the concentration ratio of PFO to BEHP-PPV, or BEHP-PPV to MEH-PPV. ^[c] For **Grating-4/5/6/7**, ten series of gratings with different periods are placed side by side to form a grating area of 300 μm × 300 μm.

Conclusion

In conclusion, we have presented a fundamental strategy to design organic semiconductor materials with wide tuning of gain bandwidth. The strategy, which involves the construction of FRET-assisted guest-host gain systems, provides convenient access to full-colour-tunable semiconductor lasers. The key to our achieved results lies in the manipulation of energy transfer efficiency that changes the energy environments for light amplification, which is elucidated by our experimental and theoretical investigations. These results will accelerate the development of next generation semiconductor materials with wide tuning of gain bandwidth that may revolutionize the fields of full-colour displays, multi-colour security tag/sensing, visible colour communications, and solid-state lighting, taking advantage of the flexibility and processability of organic electronics.

References

1. Yan, R., Gargas, D. & Yang, P. Nanowire photonics. *Nat. Photonics* **3**, 569-576 (2009).
2. Clark, J. & Lanzani, G. Organic photonics for communications. *Nat. Photonics* **4**, 438-446 (2010).
3. Hill, M. T. & Gather, M. C. Advances in small lasers. *Nat. Photonics* **8**, 908-918 (2014).
4. Eaton, S. W., Fu, A., Wong, A. B., Ning, C-Z. & Yang, P. Semiconductor nanowire lasers. *Nat. Rev. Mater.* **1**, 16028 (2016).
5. Qian, F. et al. Multi-quantum-well nanowire heterostructures for wavelength-controlled lasers. *Nat. Mater.* **7**, 701-706 (2008).
6. Pan, A. et al. Continuous alloy-composition spatial grading and superbroad wavelength-tunable nanowire lasers on a single chip. *Nano Lett.* **9**, 784-788 (2009).
7. Fan, F., Turkdogan, S., Liu, Z., Shelhammer, D. & Ning, C-Z. A monolithic white laser. *Nat. Nanotechnol.* **10**, 796-803 (2015).
8. Xing, G. et al. Low-temperature solution-processed wavelength-tunable perovskites for lasing. *Nat. Mater.* **13**, 476-480 (2014).
9. Zhu, H. et al. Lead halide perovskite nanowire lasers with low lasing thresholds and high quality factors. *Nat. Mater.* **14**, 636-642 (2015).
10. Fu, Y. et al. Broad wavelength tunable robust lasing from single-crystal nanowires of Cesium lead halide perovskites (CsPbX_3 , X = Cl, Br, I). *ACS Nano* **10**, 7963-7972 (2016).
11. Ning, C-Z., Dou, L. & Yang, P. Bandgap engineering in semiconductor alloy nanomaterials with widely tunable compositions. *Nat. Rev. Mater.* **2**, 17070 (2017).
12. Tang, C. W. & VanSlyke, S. A. Organic electroluminescent diodes. *Appl. Phys. Lett.* **51**, 913-915 (1987).
13. Burroughes, J. H. et al. Light-emitting diodes based on conjugated polymers. *Nature* **347**, 539-541 (1990).

14. Baldo, M. A. et al. Highly efficient phosphorescent emission from organic electroluminescent devices. *Nature* **395**, 151-154 (1998).
15. Uoyama, H., Goushi, K., Shizu, K., Nomura, H. & Adachi, C. Highly efficient organic light-emitting diodes from delayed fluorescence. *Nature* **492**, 234-238 (2012).
16. McGehee, M. D. & Heeger, A. J. Semiconducting (conjugated) polymers as materials for solid-state lasers. *Adv. Mater.* **12**, 1655-1668 (2000).
17. Samuel, I. D. W. & Turnbull, G. A. Organic semiconductor lasers. *Chem. Rev.* **107**, 1272-1295 (2007).
18. Kuehne, A. J. C. & Gather, M. C. Organic lasers: recent developments on materials, device geometries, and fabrication techniques. *Chem. Rev.* **116**, 12823-12864 (2016).
19. Jiang, Y. et al. Organic solid-state lasers: a materials view and future development. *Chem. Soc. Rev.* **49**, 5885-5944 (2020).
20. Schneider, D. et al. Ultrawide tuning range in doped organic solid-state lasers. *Appl. Phys. Lett.* **85**, 1886-1888 (2004).
21. Yap, B. K., Xia, R., Campoy-Quiles, M., Stavrinou, P. N. & Bradley, D. D. C. Simultaneous optimization of charge-carrier mobility and optical gain in semiconducting polymer films. *Nat. Mater.* **7**, 376-380 (2008).
22. Berdin, A., Rekola, H., Sakhno, O., Wegener, M. & Priimagi, A. Continuously tunable polymer membrane laser. *Opt. Express* **27**, 25634-25646 (2019).
23. Sandanayaka, A. S. D. et al. Indication of current-injection lasing from an organic semiconductor. *Appl. Phys. Express* **12**, 061010 (2019).
24. Karunathilaka, B. S. B. et al. Suppression of external quantum efficiency rolloff in organic light emitting diodes by scavenging triplet excitons. *Nat. Commun.* **11**, 4926 (2020).

25. Kozlov, V. G., Bulović, V., Burrows, P. E. & Forrest, S. R. Laser action in organic semiconductor waveguide and double-heterostructure devices. *Nature* **389**, 362-364 (1997).
26. Berggren, M., Dodabalapur, A., Slusher, R. E. & Bao, Z. Light amplification in organic thin films using cascade energy transfer. *Nature* **389**, 466-469 (1997).
27. Cerdán, L. et al. FRET-assisted laser emission in colloidal suspensions of dye-doped latex nanoparticles. *Nat. Photonics* **6**, 621-626 (2012).
28. Kim, D-H. et al. High-efficiency electroluminescence and amplified spontaneous emission from a thermally activated delayed fluorescent near-infrared emitter. *Nat. Photonics* **12**, 98-104 (2018).
29. Jiang, Y. et al. Low-threshold organic semiconductor lasers with the aid of phosphorescent Ir(III) complexes as triplet sensitizers. *Adv. Funct. Mater.* **29**, 1806719 (2019).
30. Belton, C. R. et al. Location, location, location - strategic positioning of 2,1,3-benzothiadiazole units within trigonal quaterfluorene-truxene star-shaped structures. *Adv. Funct. Mater.* **23**, 2792-2804 (2013).
31. Amarasinghe, D., Ruseckas, A., Vasdekis, A. E., Turnbull, G. A. & Samuel, I. D. W. High-gain broadband solid-state optical amplifier using a semiconducting copolymer. *Adv. Mater.* **21**, 107-110 (2009).
32. McGehee, M. D. et al. Amplified spontaneous emission from photopumped films of a conjugated polymer. *Phys. Rev. B* **58**, 7035-7039 (1998).
33. Xia, R., Stavrinou, P. N., Bradley, D. D. C. & Kim, Y. Efficient optical gain media comprising binary blends of poly(3-hexylthiophene) and poly(9,9-dioctylfluorene-*co*-benzothiadiazole). *J. Appl. Phys.* **111**, 123107 (2012).
34. Yu, Z. et al. Novel fluorene-based copolymers containing branched 2-methyl-butyl-substituted fluorene-*co*-benzothiadiazole units for remarkable optical gain enhancement in green-yellow

- emission range. *J. Phys. Chem. C* **120**, 11350-11358 (2016).
35. Zhou, X. et al. Low optical loss amplified spontaneous emission and lasing in a solution-processed organic semiconductor. *Adv. Opt. Mater.* **7**, 1900701 (2019).
36. Virgili, T. et al. Understanding fundamental processes in poly(9,9-dioctylfluorene) light-emitting diodes via ultrafast electric-field-assisted pump-probe spectroscopy. *Phys. Rev. Lett.* **90**, 247402 (2003).
37. Virgili, T., Marinotto, D., Lanzani, G. & Bradley, D. D. C. Ultrafast resonant optical switching in isolated polyfluorenes chains. *Appl. Phys. Lett.* **86**, 091113 (2005).
38. Zhang, Q. et al. Host exciton confinement for enhanced Förster-transfer-blend gain media yielding highly efficient yellow-green lasers. *Adv. Funct. Mater.* **28**, 1705824 (2018).
39. Ou, Q., Peng, Q. & Shuai, Z. Computational screen-out strategy for electrically pumped organic laser materials. *Nat. Commun.* **11**, 4485 (2020).
40. International Electrotechnical Commission. *Multimedia systems and equipment-colour measurement and management-Part 2-1: colour management-default RGB colour space-sRGB*, IEC 61966-2-1 (International Electrotechnical Commission, 1999).

Data availability

The data that support the plots within this paper and other findings of this study are available from the corresponding author upon reasonable request.

Acknowledgements

Financial support from Hong Kong Government ITC project (ITS/174/18) and Hong Kong Baptist University interdisciplinary project (IRCMS/19-20/H01) are gratefully acknowledged. We thank K. M. Fung and Y. Huang for their assistance in sample preparation. Q. W. thanks the support from the

Natural Science Foundation of China (61904152). The authors acknowledge the Science and Technology Development Fund, Macao SAR (File No. FDCT-0044/2020/A1, FDCT-091/2017/A2, FDCT-014/2017/AMJ), UM's research fund (File No. MYRG2018-00148-IAPME), the Natural Science Foundation of China (61935017), Natural Science Foundation of Guangdong Province, China (2019A1515012186), and Guangdong-Hong Kong-Macao Joint Laboratory of Optoelectronic and Magnetic Functional Materials (2019B121205002).

Author contributions

Y. J. and K. W. C. conceived the idea and designed the experiments. Y. J. developed the basic concepts, prepared the samples, and conducted the tunable ASE and lasing characterizations. Q. W. and G.-C. X. conducted the TA and TRPL experiments. M. Jin, K. F. L. and G. L. fabricated and characterized the DFB gratings. H. L. T. assisted with the sample preparation and characterization in ASE and lasing measurements. Y. J. and K. W. C. analysed all the results and wrote the manuscript. All authors discussed the results and commented on the manuscript at all stages. K. W. C. led the project.

Additional information

Supplementary information is available in the online version of the paper. Reprints and permission information is available online at www.nature.com/reprints.

Correspondence and requests for materials should be addressed to G.-C. X. or K. W. C.

Competing interests

The authors declare no competing interests.

Methods

Sample fabrication. PFO ($M_w=1.2 \times 10^5$) was purchased from Luminescence Technology Corp. BEHP-PPV ($M_n=6 \times 10^4 - 10 \times 10^4$) and MEH-PPV ($M_n=4 \times 10^4 - 7 \times 10^4$) were purchased from Sigma-Aldrich. All polymers were used directly without additional purification. PFO and BEHP-PPV were dissolved in toluene with different concentrations. MEH-PPV solutions were prepared with different concentrations in chloroform. The blended polymer solutions were then provided. The films for optical and ASE measurements were spin-coated on quartz with thicknesses within 120-180 nm.

Steady-state optical measurements. Shimadzu UV-3150 spectrophotometer was used to measure UV-vis absorption spectra. Shimadzu RF-5300PC spectrofluorimeter was used to record fluorescence spectra with a light source of a xenon lamp. A 0.5 m monochromator connected with a PMT was used to collect the emission signal. PLQYs of the samples in solid-state were measured by using PFO film ($\eta = 0.5$) as a calibration standard with an excitation light wavelength of 390 nm²¹. Refractive indices were measured by using a SOPRA variable angle spectroscopic ellipsometer.

TRPL measurements. For femtosecond optical spectroscopy experiments, the laser source is a Coherent Legend Elite regenerative amplifier (100 fs, 1 KHz, 800 nm) seeded by a Coherent Vitesse oscillator (100 fs, 80 MHz). 800 nm wavelength laser pulses are from the regenerative amplifier, while 400 nm wavelength laser pulses are obtained through a BBO doubling crystal. The 400 nm laser pulses with a spot diameter of 2 mm were incident to the films. The emission from the samples were collected at a backscattering angle of 150° by a pair of lenses into an optical fiber that was coupled to a spectrometer (Acton, Spectra Pro 2500i) and detected by a charge coupled device (CCD, Princeton Instruments, Pixis 400B). Transient PL was collected by using an Optronis Optoscope streak camera system which has an ultimate temporal resolution of ~10 ps.

TA experiments. The broadband femtosecond TA spectra of the blended films were taken by using

the Ultrafast System HELIOS TA spectrometer. The laser source for TA experiments was the same source in TRPL measurements. The broadband probe pulses (420-800 nm) were generated by focusing a small portion (around 10 mJ) of the fundamental 800 nm laser pulses into a 2 mm sapphire plate. The 400 nm pump pulses were obtained through doubling the fundamental 800 nm pulses with a BBO crystal. We fitted the TA kinetics according to a multi-exponential decay function,

$$I(t) = 1/2 \sum_{i=1}^N H_i(t) A_i \exp\left(-\frac{t}{\tau_i}\right) \quad (1)$$

where t is the probe time delay, $H_i(t) = [1 + \text{erf}(-t/r - r/2\tau_i)]$ (erf: error function) is the rising function, r (~ 0.1 ps) is the Gaussian laser pulse width, A_i is the amplitude or pre-exponential function, and τ_i is the decay time.

Simulations. The stimulated emission cross-section ($\sigma_{\text{em}}(\lambda)$) is deduced from the Einstein A and B coefficients. It can be determined as⁴¹,

$$\sigma_{\text{em}}(\lambda) = \frac{\lambda^4 E_f(\lambda)}{8\pi n^2(\lambda) c \tau_f} \quad (2)$$

where $E_f(\lambda)$ is the PL quantum distribution (at different emission wavelength), $n(\lambda)$ is the refractive index (at different emission wavelength), c is the vacuum light velocity, and τ_f is the fluorescence lifetime. The parameters for simulations at each radiative channel are depicted in Supplementary Section 5. The results of $\sigma_{\text{em}}(\lambda)$ of BEHP-PPV:MEH-PPV blend system are shown in Supplementary Fig. 25.

The existence of re-absorption, singlet-singlet excited state absorption, charge absorption, and triplet-triplet excited state absorption is known to affect the light amplification properties^{2, 18, 19}. Therefore, the effective $\sigma_{\text{em}}(\lambda)$ ($\sigma_{\text{em, eff}}(\lambda)$) is defined by the following equation^{39, 42},

$$\sigma_{\text{em, eff}}(\lambda) = \sigma_{\text{em}}(\lambda) - \sigma_{\text{abs}}(\lambda) - \sigma_{\text{S-S}}(\lambda) - \sigma_{\text{charge}}(\lambda) - \sigma_{\text{T-T}}(\lambda) \quad (3)$$

where σ_{abs} is absorption cross-section of the ground-state species, $\sigma_{\text{S-S}}$ is absorption cross-section of the singlet-singlet excited-state species, σ_{charge} is charge absorption cross-section, and $\sigma_{\text{T-T}}$ is triplet-

triplet excited-state absorption cross-section. Due to the negligible overlap between host PIA and effective gain regions from TA measurements, σ_{S-S} , σ_{charge} and σ_{T-T} at each selected emission wavelength are almost zero in BEHP-PPV:MEH-PPV blend system. The calculations of σ_{abs} are using the method reported by W. Holzer, et al.⁴³ The results of $\sigma_{\text{em, eff}}(\lambda)$ are shown in Supplementary Fig. 26. As a result, the contribution ratios of $\sigma_{\text{em, eff}}(\lambda)$ at different colours, i.e., sky-blue, green, yellow, and red, from possible radiative channels in both guest and host are shown in Supplementary Fig. 27.

ASE and lasing characterization. For ASE measurements, the pumped laser pulses were provided by the third harmonic (355 nm) of a Nd:YAG laser (5 ns, 10 Hz). A cylindrical lens was used to transform the laser beam into a 5.0 mm × 0.35 mm stripe shaped excitation area. The edge ASE emission was monitored with an Oriel Instrument fiber-coupled spectrograph equipped with a CCD detector. The ASE threshold values were estimated without taking account of transmission losses. For 1D DFB laser fabrications, the gratings with different periods were prepared using electron beam lithography on fused silica substrates. The gain media were then spin-coated on the top. 1D DFB lasers were optically pumped with the same light source with a spot radius of ~100 μm. The incident pulse energy on the sample was adjusted by the continuously variable neutral density filter into the beam path, which was detected by Power meter PM100D (Thorlabs). The sample was normal to the incident pump laser beam. The transmitted pump laser was cut off by placing filter BG38 behind the sample. The laser spectra were collected by the fiber spectrometer (Ocean Optics USB4000-US-VIS).

References

41. Webb, J. P., McColgin, W. C., Peterson, O. G., Stockman, D. L. & Eberly, J. H. Intersystem crossing rate and triplet state lifetime for a lasing dye. *J. Chem. Phys.* **53**, 4227-4229 (1970).
42. Aoki, R. et al. Realizing near-infrared laser dyes through a shift in excited-state absorption. *Adv. Opt. Mater.* **9**, 2001947 (2021).

43. Holzer, W. et al. Amplified spontaneous emission in neat films of arylene-vinylene polymers.
Opt. Quantum Electron. **33**, 121-150 (2001).

Supplementary Files

This is a list of supplementary files associated with this preprint. Click to download.

- [JYSupplementaryInformationTunableLaser210419forNatPhotonics.docx](#)